Radiation-Induced Metabolic Reprogramming of Fibroblasts Regulates the Breast Cancer Microenvironment

Kevin C. Corn[1], Lucy S. Britto[2], Yoanna I. Ivanova[2], Youssef K. Mohamed[1], and Marjan Rafat[1,2,3,*]

[1]Department of Chemical and Biomolecular Engineering, Vanderbilt University, Nashville, TN, USA

[2]Department of Biomedical Engineering, Vanderbilt University, Nashville, TN, USA

[3]Department of Radiation Oncology, Vanderbilt University Medical Center, Nashville, TN, USA

*Author for correspondence: Marjan Rafat, Engineering and Science Building, Rm. 426, Vanderbilt University, Nashville, TN 37212. Phone: (615) 343-3389, Fax: (615) 343-7951, E-mail: marjan.rafat@vanderbilt.edu

Summary

Although radioresistant and circulating tumor cell survival has been attributed to altered metabolic profiles, the metabolic impact of radiation therapy on normal stromal cells is poorly understood. The authors provide a mechanism for post-radiotherapy metabolic crosstalk between radiation-damaged fibroblasts and triple negative breast cancer cells that may influence recurrence.

Abstract

Triple negative breast cancer (TNBC) patients continue to have high recurrence rates despite current treatment modalities, including radiation therapy (RT). Radiation-resistant TNBC cells and circulating tumor cells thought to be involved in recurrence survive in part due to changes in their metabolic profiles. These tumor cells interact with radiation-damaged stromal cells such as fibroblasts following treatment. How fibroblasts metabolically respond to RT and metabolically crosstalk with TNBC cells is poorly understood. In this study, we identified that radiation-damaged fibroblasts accumulate lipids up to 7-days following treatment due to increased autophagic flux. This lipid accumulation and autophagy allows fibroblasts to maintain increased fatty acid oxidation, overall mitochondrial respiration, and aerobic glycolysis rates. TNBC cells responded by decreasing autophagy and increasing ATP-linked respiration and migration rates. Our work highlights how metabolic crosstalk between radiation-damaged fibroblasts and TNBC cells leads to a microenvironment conducive to recurrence.

Graphical Abstract

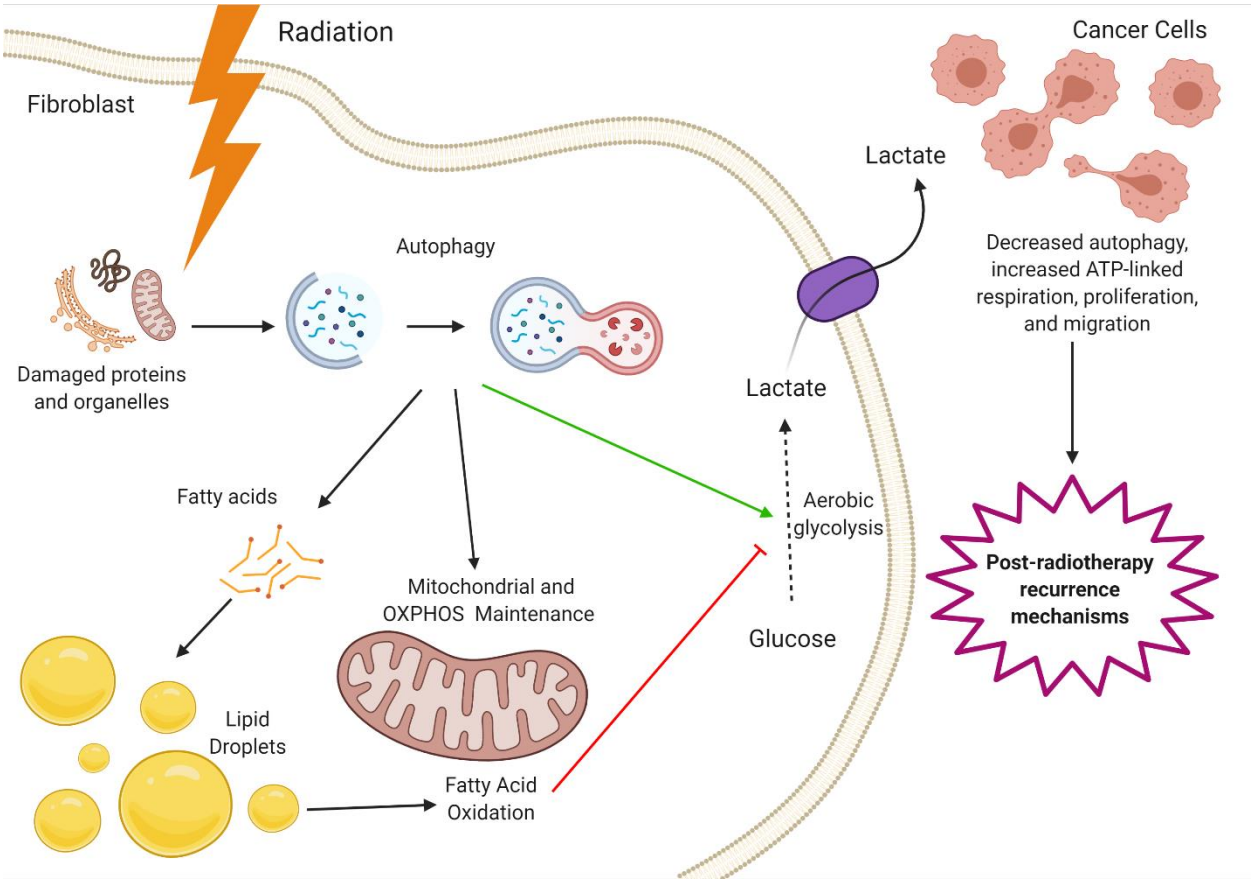

Abbreviations

ATP: Adenosine triphosphate

CAF: Cancer associated fibroblast

CM: Conditioned media

CPT1A: Carnitine palmitoyl transferase 1a

CTC: Circulating tumor cell

ECAR: Extracellular acidification rate

ECM: Extracellular matrix

FAO: Fatty Acid Oxidation

FASN: Fatty acid synthase

IF: Immunofluorescence

LC3B: Microtubule-associated protein 1A/1B-light chain 3 B

MCT: Monocarboxylate transporter

NAT: Normal adjacent tissue

OXPHOS: Oxidative phosphorylation

OCR: Oxygen consumption rate

ROS: Reactive oxygen species

RT: Radiation therapy

TME: Tumor microenvironment

TNBC: Triple negative breast cancer

Introduction

Breast cancer is the most diagnosed cancer worldwide, with an estimated 2.3 million new cases, and remains one of the most deadly forms of cancer for women[1]. Roughly 15% of all breast cancer diagnoses will be for triple negative breast cancer (TNBC), a highly aggressive and metastatic subtype that disproportionately affects pre-menopausal, African American, and Hispanic women[2,3]. Treatment for TNBC typically consists of surgery, neoadjuvant chemotherapy, and adjuvant radiation therapy (RT)[4,5]. The primary goal of RT is to eliminate residual cancer cells following surgery, and it is largely effective at reducing the incidence of recurrent disease[6]. Although technology has improved drastically over the years leading to better outcomes for patients and decreased off-target effects, TNBC patients still experience high locoregional recurrence rates of up to 20%[7–10].

Residual radioresistant cancer cells adopt an altered lipid metabolic profile that may promote recurrence[11,12]. Both increased *de novo* fatty acid synthesis and fatty oxidation (FAO) are linked to radioresistance in breast and other cancers treated by radiotherapy[13–17]. In addition, the recruitment of breast circulating tumor cells (CTCs) to radiation-damaged sites has recently been identified as a contributing factor to locoregional recurrence beyond residual tumor cells in the irradiated surgical bed[18,19]. Altered lipid metabolic profiles have been shown to drive cancer cell resistance to anoikis after detachment, especially through upregulated FAO[20–22]. Understanding metabolic changes following RT may be critical in reducing recurrent disease. However, how the normal tissue cells in the adjacent tumor microenvironment respond metabolically to radiation damage and how these cells interact with residual or recruited CTCs has been largely unexplored.

Fibroblasts are major cellular players in the wound healing response to radiation damage. They are recruited to radiation-damaged sites, activated to myofibroblasts, and lay down new extracellular matrix (ECM) to promote healing[23]. Fibroblasts are found within the murine mammary gland and, at even higher amounts, in human breast tissue[24,25]. Therefore, fibroblasts within the mammary tissue will be exposed to off-target effects of RT and may interact with residual or recruited CTCs to influence recurrence. Considering the importance of altered metabolic profiles in the development of radioresistance in cancer cells, understanding how other cell types within the normal tissue metabolically respond to radiation damage is imperative for determining recurrence mechanisms. Many studies have focused on cancer-associated fibroblasts (CAFs) and their interactions with tumor cells. CAFs can transfer lipids and fatty acids to[26,27] and upregulate lipid synthesis and saturation pathways in tumor cells[28,29]. Upregulated glycolysis in CAFs also plays a critical role in tumor progression through the secretion of lactate, providing an

alternate fuel source for oxidative cancer cells[30,31]. A correlation between fibroblast metabolic profiles and ECM regulation, where glycolysis correlates to ECM deposition and lipid metabolism to ECM degradation, has been observed in fibrosis, a known outcome of radiation therapy[32]. These studies suggest that fibroblast metabolism may lead to metabolic crosstalk with tumor cells and subsequent recurrence.

Here, we studied how radiation damage alters fibroblast metabolism following RT. We determined that irradiated fibroblasts accumulate lipids for up to 7 days following irradiation due to sustained increased autophagic flux. Irradiated fibroblasts demonstrated increased ATP-linked mitochondrial respiration and extracellular acidification from glycolysis, suggesting that radiation-damaged cells are highly energetic. With high extracellular acidification rates observed 7-days post-RT, we hypothesized that lactate shuttling from irradiated fibroblasts could impact TNBC cells. We determined that high lactate secretion from irradiated fibroblasts decreased TNBC cell autophagy and increased ATP-linked mitochondrial respiration and migration rates through monocarboxylate transporters 1 and 2 (MCT1 and MCT2), all characteristics of aggressive recurrent disease. Our study demonstrates a metabolic recurrence mechanism that can be targeted to improve TNBC patient survival following RT.

Results and Discussion

Radiation damage results in tumor cell recruitment and accumulation of lipid droplets in fibroblast cells.

Since previous work demonstrated that the damaged mammary stroma can secrete factors that recruit CTCs and promote TNBC recurrence following RT[18], we evaluated whether irradiated NIH 3T3 fibroblasts could promote 4T1 TNBC cell invasion. Conditioned media (CM) was collected from fibroblasts irradiated to 10 Gy after incubation for 2 or 7 days and used in a transwell invasion assay. CM from irradiated fibroblasts significantly increased 4T1 invasion compared to CM from unirradiated control fibroblasts (**Fig 1A**). To determine the radiosensitivity of NIH 3T3 fibroblasts, a clonogenic assay was performed. NIH 3T3 fibroblasts are radioresistant when compared to 4T1 radiosensitivity as expected[19] (**Fig S1A**). γ-H2AX expression following RT to 10 Gy in 3T3s and 4T1s demonstrated similar levels of DNA damage in both cell types (**Fig S1B–C**). These results suggest that although fibroblasts may experience equivalent levels of DNA damage for the same radiation dose as cancer cells, they are more likely to survive following therapy and therefore could interact with residual or recruited TNBC cells.

Due to the importance of lipid metabolism in radioresistant cancer cells and CTCs, we hypothesized lipid droplets in fibroblasts may be a critical marker for post-RT metabolic profile

analysis and could lead insights into recurrence mechanisms. We evaluated the expression of perilipin-2, a protein found in lipid droplet membranes of many cell types[33], in the normal adjacent tissue (NAT) of breast cancer patients from the TCGA BRCA dataset[34]. We observed that patients with high levels of NAT perilipin-2 expression had worse overall survival compared to those with low expression (**Fig 1B**), demonstrating an inverse relationship between lipid droplets in the NAT and breast cancer patient survival. We next explored perilipin-2 expression in irradiated fibroblasts up to 7 days following radiation damage (**Fig 1C–D**). There was up to a 2-fold increase in lipid droplets by 7 days post-RT in irradiated cells, suggesting an altered lipid metabolic profile persists well after the initial cellular stresses of RT (**Fig 1C**). This trend was confirmed through fluorescent imaging after incubation with Nile Red, which stains the nonpolar regions of lipid droplets[35] (**Fig S1D–E**). Interestingly, we observed decreased intensity of perilipin-2 staining in the lipid droplets of irradiated fibroblasts starting at 3 days post-RT, suggesting these lipid droplets may be more susceptible to lipolysis, degradation, and utilization by the cells at these later time points (**Fig S1F**). To further confirm the trend of increased lipid accumulation in irradiated fibroblasts, we stained fibroblasts with BODIPY 493/503 and performed flow cytometry analysis (**Fig S1 G–I**). An increasing peak shift in BODIPY intensity was observed in irradiated cells compared to unirradiated control fibroblasts (**Fig 1E**).

Increased lipid storage has been demonstrated in multiple cell types following radiation damage, such as in macrophages[36] and dendritic cells[37], but this phenomenon has been observed when they have been recruited to areas of radiation damage, suggesting either extracellular fatty acid uptake or uptake of other metabolites that are utilized for *de novo* fatty acid synthesis and eventually storage in lipid droplets. We evaluated the expression of fatty acid synthase (FASN), the enzyme responsible for conversion of acetyl-CoA to palmitic acid and the rate-limiting step of *de novo* fatty acid synthesis and saw no significant differences between irradiated and unirradiated fibroblasts (**Fig S2A–B**). To test if irradiated fibroblasts were taking up increased quantities of extracellular fatty acids from serum and storing them in lipid droplets, we incubated both irradiated and control fibroblasts with BODIPY-conjugated palmitate. No significant differences in fluorescent intensity were observed between the irradiated and control fibroblasts, suggesting no upregulation of fatty acid uptake from the media (**Fig S2C–D**). Taken together, these results suggested an alternate pathway for lipid accumulation within the irradiated fibroblasts.

Radiation-induced autophagy promotes lipid droplet formation.

Radiation-induced autophagy has been demonstrated in tumor cells as a mechanism for the

removal of biomolecules and cellular compartments damaged by reactive oxygen species generated from RT[38,39]. We hypothesized that activation of autophagy in irradiated fibroblasts and the degradation of lipid membranes in damaged organelles could result in the observation of increased lipid droplet storage similar to lipid accumulation following starvation-induced autophagy[40]. We began our analysis by analyzing the presence of acidic lysosomes in live irradiated and unirradiated fibroblasts through LysoTracker Red DND-99 staining (**Fig 2A**). We observed a significant increase in lysosome formation and acidification starting at day 3 following radiation damage in irradiated fibroblasts, which persisted through 7-days post-RT (**Fig 2B**). We evaluated the formation of autophagosomes through immunofluorescence (IF) staining of microtubule-associated protein 1A/1B-light chain 3 B (LC3B)[41]. LC3B IF staining demonstrated bright puncta formation starting at day 3 following radiation damage in the irradiated cells (**Fig 2C**), which remained through 7-days post-RT (**Fig 2D**), suggesting an upregulation of autophagy during the time period of increased lipid accumulation in irradiated cells.

Although increased lysosomal staining and LC3B puncta formation may indicate increased autophagic flux, these results can also be observed in cells with defective autophagy[42] that has also been demonstrated in radiation-damaged cells[43]. To confirm if there was increased autophagic flux within the irradiated fibroblasts, we utilized the autophagy inhibitor chloroquine (CQ). CQ treatment successfully resulted in a decrease in lysosomal acidification (**Fig 2E**) at 3-days post-RT. Staining for LC3B in CQ-treated irradiated cells showed a substantial increase in LC3B positive structures, confirming that irradiated cells have increased autophagic flux at both the 3- (**Fig 2F–G**) and 7-days post-RT (**Fig S2E**). Additionally, CQ treatment of unirradiated cells showed an increase in LC3B puncta staining, indicating that normal fibroblasts have a low basal level of autophagy. Once confirming increased autophagic flux in irradiated fibroblasts, we evaluated the impact of autophagy inhibition on lipid droplet formation. Inhibition of autophagy at 3-days post-RT led to a substantial decrease in lipid droplet formation in irradiated fibroblasts from perilipin-2 IF analysis (**Fig 2H**), which was also confirmed at the 7-day post-RT timepoint (**Fig S2F**). To further confirm these results, we stained CQ-treated and untreated fibroblasts up to 7 days following RT with BODIPY and performed flow cytometry analysis. These experiments confirmed that increased lipid droplet formation in irradiated cells was abrogated by CQ treatment (**Fig 2I and Fig S2G**), suggesting prolonged autophagy upregulation in fibroblasts following radiation damage leads to an altered lipid metabolic profile.

Metabolic flux analysis reveals increased mitochondrial respiration is linked to autophagy and FAO in irradiated fibroblasts.

We stained fibroblasts with MitoTracker Deep Red to evaluate a baseline level of mitochondrial dynamics following radiation[44,45]. We observed that irradiated cells had higher mitochondrial staining (**Fig 3A–B**), especially between 5- and 7-days following radiation damage. These results indicate that irradiated fibroblasts have increased mitochondrial activity. Mitochondrial staining intensity was evaluated by flow cytometric analysis after CQ-induced inhibition of autophagy to understand the impact this process may have on recycling of damaged mitochondria. Autophagy inhibition resulted in an increase in mitochondrial staining for both irradiated and unirradiated cells, suggesting that autophagy may be important in removing damaged or dysfunctional mitochondria especially in irradiated cells (**Fig 3C**).

We then evaluated mitochondrial bioenergetics through a modified mitochondrial stress test using metabolic flux analysis with autophagy inhibition (**Fig S3A–B**). Irradiated fibroblasts had a roughly 2-fold increase in ATP-linked oxygen consumption rate (OCR) compared to unirradiated fibroblasts **(Fig 3D)**, matching observations of increased mitochondrial staining. Although autophagy inhibition resulted in a substantial increase in MitoTracker staining in fibroblasts, autophagy inhibition appeared to cause a significant reduction in the OCR profiles in irradiated fibroblasts similar to unirradiated controls (**Fig S3A**). Additionally, the large ATP-linked OCR of irradiated fibroblasts was completely abrogated upon autophagy inhibition (**Fig 3D**). These results indicate that increases in CQ-induced mitochondrial staining in fibroblasts are related to an increase in defective mitochondrial biomass and not increased membrane potential, confirming that increased autophagy observed in irradiated fibroblasts is critical for recycling damaged mitochondria and maintaining higher mitochondrial respiration.

We next examined whether the higher basal and mitochondrial-linked OCRs in irradiated fibroblasts were the result of increased FAO from the post-radiation increase in lipid droplet stores. We performed the mitochondrial stress test with the addition of etomoxir to inhibit carnitine palmitoyl transferase 1a (CPT1A), the transporter involved in the rate-limiting step in FAO that allows for the transport of long-chain fatty acids into the mitochondria. We observed a statistically significant reduction in OCR rates following incubation of etomoxir at 7-days post-RT (**Fig 3E, S3C**). This suggests that FAO is occurring in irradiated cells, but it is not responsible for the entirety of the observed ATP-linked OCR increases. We further confirmed this effect by analyzing BODIPY intensity changes following etomoxir treatment in irradiated and unirradiated fibroblasts. An increase in BODIPY intensity in irradiated cells treated with etomoxir further supports increased FAO rates in irradiated fibroblasts (**Fig 3F**).

We also observed a shift in the extracellular acidification rate (ECAR) in irradiated cells during the modified mitochondrial stress test with and without CQ inhibition (**Fig S3B**). At 3-days

post-RT, irradiated and unirradiated fibroblasts exhibited equivalent basal ECAR; however, after 7-days, irradiated fibroblasts exhibited an almost 2-fold higher basal ECAR, which required autophagy in order to be maintained (**Fig 3G**). Additionally, if fibroblasts were prevented from utilizing FAO through etomoxir injection, ECAR was also decreased (**Fig S3D**). This suggests an increase in aerobic glycolysis in irradiated fibroblasts at late timepoints following radiation damage, increased rates of which can only be maintained as a result of post-radiation induced autophagy or FAO. We confirmed that irradiated fibroblasts had higher glycolytic ECAR compared to unirradiated fibroblasts in response to a bolus of glucose in saturating levels of glutamine (**Fig 3H**, **S3E–F**). This increase in aerobic glycolysis was further supported by an increase in intracellular pyruvate levels in 7-day post-RT irradiated fibroblast lysates compared to unirradiated controls (**Fig S3G**). Notably, Ki67 staining of irradiated and control fibroblasts up to 7-days post-RT showed a substantial decline in Ki67-positive cells within the irradiated fibroblast population, suggesting increased aerobic glycolysis was not the result of the selection of a radioresistant proliferating fibroblast population (**Fig S3H**).

Increased radiation-induced aerobic glycolysis in fibroblasts promotes lactate secretion and metabolic crosstalk with TNBC cells.

We incubated TNBC cells with fibroblast CM collected from 7-day post-RT fibroblasts and observed decreased LysoTracker live cell staining intensity (**Fig 4A, S3I**) and decreased autophagosome formation (**Fig 4A, S3J**) in the TNBC cells, suggesting a metabolite specifically from irradiated fibroblasts decreases basal levels of autophagy in TNBC cells. Considering 7-day post-RT irradiated fibroblasts demonstrated increased aerobic glycolysis, we hypothesized that the metabolite responsible for decreased autophagy in TNBC cells was lactate. Indeed, 7-day post-RT irradiated fibroblast CM contained over a 2-fold increase in L-lactate concentration compared to unirradiated CM (**Fig 4C**). In the tumor microenvironment, CAFs adopt a glycolytic metabolic profile that results in lactate secretion and transfer to breast cancer cells, fueling the TCA cycle and increasing breast cancer bioenergetics[30,31]. We evaluated mitochondrial energetics in CM-incubated TNBC cells and saw an almost 50% increase in ATP-linked OCR for the irradiated CM condition (**Fig 4D, S3K**), suggesting TNBC cells were increasing lactate uptake and this lactate was being utilized for ATP generation that could impact energy intensive processes. Lactate is transported into and out of cells through monocarboxylate transporters (MCTs), where MCT4 is the major lactate exporter and MCT1 and MCT2 are responsible for uptake[46]. To block lactate uptake by TNBC cells, we utilized the MCT1/2 small molecule inhibitor AZD3965, which has been utilized in phase 1 breast cancer clinical trials[47]. High levels of

AZD3965 reduced basal proliferation of TNBC cells substantially (**Fig S3L**). Lactate uptake in TNBC cells was reduced by approximately 100% with 50 nM of AZD3965, which we then used in our lactate crosstalk studies (**Fig S3M**).

We first evaluated the impact of lactate uptake inhibition on TNBC autophagy. As anticipated, decreased lactate uptake substantially increased both lysosomal acidification (**Fig 4E**) and autophagosome formation (**Fig 4F**) in irradiated fibroblasts, confirming lactate was the metabolite decreasing basal levels upon initial incubation with irradiated fibroblast CM. As TNBC cells in irradiated fibroblast CM had increased ATP-linked OCR rates, we hypothesized lactate uptake could impact TNBC cell migration. We conducted a scratch-wound assay (**Fig 4G**) where TNBC cells were exposed to either 7-day post-RT irradiated or unirradiated fibroblast CM and the closure of the gap was observed over 15 hours. TNBC cells incubated in irradiated fibroblast CM closed the gap at a significantly higher rate compared to TNBC cells in unirradiated fibroblast CM. With the addition of 50 nM AZD3965, the closure time was substantially reduced (**Fig 4H**). This suggests that increased lactate secretion from irradiated fibroblasts enhanced migration rates of TNBC cells. We next looked at a co-culture between fibroblasts and TNBC cells to understand if there was a proliferative impact on TNBC cells when in contact with irradiated fibroblasts. TNBC cells co-cultured with irradiated fibroblasts demonstrated increased bioluminescence signal compared to those co-cultured with unirradiated fibroblasts, suggesting increased proliferation rates (**Fig 4I**). This combined impact of decreased autophagy, increased migration, and increased proliferation in TNBC cells suggests fibroblasts can induce an aggressive phenotype in TNBC cells following RT that could impact patient prognosis.

In our experiments, we found a link between post-radiation lipid accumulation in lipid droplets, radiation-induced autophagy, aerobic glycolysis, and lactate metabolic crosstalk between irradiated fibroblasts and TNBC cells. To determine the connection between these mechanisms in human tissue, we revisited our patient NAT analysis. We evaluated gene expression data for *Map1lc3b* (LC3B), lipase A (*Lipa*), and lactate dehydrogenase (*Ldha*). We found strong correlations with the expression of each of these genes against expression of *Plin2* (**Fig 4J**), which also correlated with overall worse survival for breast cancer patients (**Fig. 1B**). These analyses further suggest that radiation-induced autophagy, lipid droplet formation, aerobic glycolysis, and lactate secretion by fibroblasts may contribute to post-RT recurrence mechanisms.

In summary, we provide a link between post-radiation metabolic alterations in fibroblasts and metabolic crosstalk that leads to an aggressive TNBC phenotype. This work demonstrates how radiation damage to normal tissue cells may impact TNBC recurrence mechanisms.

Materials and Methods

Cell culture. NIH 3T3 murine embryonic fibroblasts were obtained from ATCC and cultured in high glucose DMEM (Gibco 11995-065) containing 10% bovine calf serum and 1% penicillin/streptomycin. Luciferase-labeled 4T1 mouse mammary carcinoma cells ($4T1^{luc}$) were obtained from Dr. Christopher Contag (Stanford University) in August 2011, and unlabeled 4T1 cells were obtained from ATCC. 4T1 cells were cultured in RPMI 1640 medium (Gibco11875-093) containing 10% heat-inactivated fetal bovine serum and 1% penicillin/streptomycin. All cells were maintained at 37°C in a humified incubator containing 5% CO_2.

Radiation. For radiation experiments, NIH 3T3 fibroblasts were grown to 70% confluency in T75 or T25 flasks and then irradiated up to a dose of 10 Gy using a cesium source. Cells were immediately plated. Cell counts at the indicated post-RT timepoints were kept constant between irradiated and non-irradiated cells.

Clonogenic assays and DNA damage analysis. NIH 3T3 fibroblasts were irradiated to doses up to 10 Gy and plated in 6 cm dishes in normal growth media in triplicate at appropriate concentrations. After 12 days, colonies were stained with 0.25% w/v crystal violet solution in 95% ethanol and counted. The survival data was fitted with the linear-quadratic model (Surviving Fraction $= e^{-(\alpha * Dose + \beta * Dose^2)}$). For DNA damage analysis, cells on glass coverslips were irradiated to doses up to 10 Gy. Cells were fixed for immunofluorescence staining of γ-H2AX 30 minutes following RT[48,49].

Fibroblast conditioned media (CM). Irradiated and unirradiated fibroblasts were plated in T75 or T25 flasks in complete growth media for either 2 or 7 days, at which point supernatant was collected and filtered through a 0.2 μm filter to remove any cell debris. Cell counts between irradiated and unirradiated flasks at the time of CM collection were kept consistent. Filtered CM was stored at –80°C until use. L-lactate concentration in CM was determined using an EnzyFluo™ L-lactate assay kit (Bioassay Systems EFLLC-100) following the manufacturer's instructions. 4T1 cells were incubated in fibroblast CM, and normal media was removed 24 hours prior to 70% confluency and replaced with CM for incubation at 37°C.

Invasion assays. CM from NIH 3T3s were used as chemoattractants in a transwell invasion assay. 1×10^5 $4T1^{luc}$ cells were placed in upper chambers of migration (Corning, BioCoat PET control inserts, 8 μm pore size) or invasion inserts (Corning, BioCoat growth-factor reduced

Matrigel invasion matrix, 8 µm pore size) and were allowed to migrate toward the chemoattractant for 24 hours, and cells that migrated or invaded through membranes were fixed in methanol, mounted on slides with ProLong glass antifade mountant with NucBlue stain (Invitrogen P36981), and counted. Migration was confirmed by imaging the $4T1^{luc}$ cells that migrated through the membrane to the 24-well receiver plate using bioluminescence imaging. For biolumescence readings, an IVIS Lumina Series III (Caliper LifeSciences) was used. Cells were imaged after incubation with 0.167 mg/mL Luciferin (Biosynth L-8220) for 10 minutes.

TCGA patient data analysis. The TCGA TARGET GTEx study was accessed through the University of California Santa Cruz's Xena platform on March 31st, 2022 to evaluate how gene expression of *Plin2* in the normal adjacent tissue (NAT) of breast cancer patients correlated with overall survival, and to analyze co-expression with *Map1lc3b, Lipa, and Ldha*[34]. The Xena visualization tool was utilized (https://xenabrowser.net/) to first access the TCGA TARGET GTEx dataset, and then only Solid Tissue Normal sample types under the TCGA study label were kept for analysis. Subsequently, "Breast" was selected as the primary site to only include patient data from TCGA from breast cancer patients. These selections yielded a total patient dataset of n = 113 NAT samples. *Plin2* was then entered to evaluate gene expression data via RNAseq analysis, and a Kaplan Meier curve was generated utilizing the built-in functionality of the Xena platform. *Map1lc3b, Lipa, and Ldha* were subsequently entered to collect gene expression data and evaluation linear correlation with *Plin2*, where Pearson correlation coefficients were calculated.

Lipid droplet staining. Nile Red (Invitrogen N1142) and BODIPY 493/503 (Invitrogen D3922) fluorescent dyes were used for neutral lipid detection in cells. For Nile Red, cells were incubated with 5 µg/mL solution following fixation in neutral-buffered formalin for 20 minutes at 4°C and then washed in PBS prior to mounting with ProLong Glass Antifade Mountant with NucBlue Stain. For BODIPY 493/503, cells were labeled with a 2 µM solution for 30 minutes at 37°C[50].

Immunofluorescence. For staining requiring permeabilization, cells fixed in neutral-buffered formalin were incubated in a 0.1% Triton X-100 solution (Sigma X100) for 10 minutes. For LC3B staining, cells were fixed in 100% ice-cold methanol for 10 minutes at -20°C. Cells were blocked for 1 hour at room temperature with 10% normal goat serum (Vector Labs S-1000) and then incubated overnight at 4°C in a humidified chamber with anti-phospho-histone H2A.X (1:500, Invitrogen MA5-38225), anti-perilipin-2 (1:200, Invitrogen MA5-32664), anti-FASN (1:50, Invitrogen MA5-14887), anti-LC3B (1:200, Abcam ab192890), and anti-Ki67 (1:200, Invitrogen

MA5-14520) in 1% bovine serum albumin (Sigma A1470) and 0.1% Tween-20 (Sigma P1379). Coverslips were mounted onto slides using ProLong Glass Antifade Mountant with NucBlue following secondary antibody incubation with goat anti-rabbit IgG AlexaFluor 488 (1:200, Invitrogen A-11008) or goat anti-rabbit IgG AlexaFluor 594 (1:200, Invitrogen A-11012). A corresponding no primary antibody control was performed for all conditions to confirm specificity.

Microscopy. Microscopy images were acquired using a Leica DMi8 inverted microscope and Leica DFC9000GT sCMOS fluorescence microscope camera. For fluorescence microscopy, a Lumencor mercury-free SOLA light engine was used for the illumination source. For live cell imaging, cells were imaged using an Okolab Bold Line CO_2 and temperature unit with air pump. The microscope was fitted with DAPI, GFP, TXR, and Y5 filter cubes. Images (8 bit) were captured using LASX imaging software and analyzed using ImageJ. Z-stacks were merged using max intensity projections.

BODIPY-labeled palmitate uptake experiments. BODIPY FL C_{16} (4,4-Difluoro-5,7-Dimethyl-4-Bora-3a,4a-Diaza-*s*-Indacene-3-Hexadecanoic Acid, Invitrogen D3821) was used to assess ability to transport fatty acids from their surroundings. Uptake experiments were performed following pre-established protocols with slight modifications[51]. Briefly, fibroblasts were washed in serum-free media and incubated in 10 µM BODIPY FL C_{16} for 5 minutes at 37°C. Cells were then washed with serum-free media and incubated with 1.5 µM of Hoechst 33345 (ThermoScientific) for 20 minutes. Cells were imaged in Hank's buffered saline solution (HBSS, Corning 21-023-CV). The relative amount of BODIPY FL C_{16} taken up by irradiated and unirradiated control cells was determined by the quantification of the integrated density normalized by cell count using ImageJ.

Lysosome imaging. LysoTracker Red DND-99 (Invitrogen L7528) was used to identify lysosomal structures in 3T3 and 4T1 cells. Cells were seeded in tissue-culture treated 24-well plates at appropriate seeding densities based on the timepoint post-RT and incubated with 50 nM of LysoTracker Red DND-99 and 1.5 µM of Hoechst 33345 solution in media for 30 minutes at 37°C. Following incubation, cells were washed with and imaged in HBSS. Positive lysosomal staining was determined by quantifying the integrated density using ImageJ software and normalizing by the number of cells per field of view.

Autophagy inhibition and autophagosome analysis. Irradiated or unirradiated NIH 3T3 cells were seeded on glass coverslips at appropriate seeding densities based on the timepoint post-

RT. Chloroquine diphosphate salt (Sigma C6628) was used as an autophagy inhibitor. At 5 hours prior to the post-RT timepoint, cells were incubated with 100 μM of chloroquine in cell culture media. Control cells were treated with equivalent volumes of PBS. After 5 hours of inhibition[52], cells were washed and either fixed for immunofluorescence staining, imaged live for Lysotracker experiments, collected for flow cytometry analysis, or prepared for metabolic flux analysis. For autophagosome analysis, 3T3 or 4T1 cells were stained for LC3B as described previously. The formation of bright puncta compared to diffuse LC3B IF staining in the cytoplasm was considered to be the formation of autophagosomes[41]. These puncta were analyzed by thresholding after subtracting background fluorescence using ImageJ, and the cross-sectional area per cell was calculated to represent the number of autophagosomes in the cell. An increase in autophagosomes following chloroquine inhibition was used as a confirmation of autophagic flux.

Mitochondrial staining. MitoTracker Deep Red (Invitrogen M22426) was used to evaluate mitochondria in 3T3 cells. Stock powder was dissolved in DMSO and used at a working concentration of 200 nM. Prior to staining, cells were washed with PBS and stained with MitoTracker Deep Red and a 1.5 μM Hoechst 33345 solution (for plate-reader analysis) in serum-free media for 30 minutes at 37°C. Following incubation, cells were washed twice with complete media and then either prepared for flow cytometry analysis or washed and placed in HBSS for imaging using a Varioskan LUX plate reader (Thermo Scientific).

Flow cytometry. Fibroblasts were analyzed via flow cytometry to evaluate BODIPY staining for lipid droplets and MitoTracker Deep Red staining for mitochondrial membrane potential following RT, autophagy inhibition (100 μM CQ for 5 hours), and FAO inhibition (40 μM etomoxir sodium salt hydrate, Sigma E1905, 5 hour inhibition). At the appropriate timepoints following RT and/or inhibition, cells were stained for MitoTracker Deep Red and BODIPY for 30 minutes at 37°C. Cells were trypsinized, pelleted, and resuspended in ice-cold PBS at a concentration of $1x10^6$ cells/mL. Cells were placed on ice and stained for live cells using a live/dead aqua viability kit (Life Technologies L34966) following the manufacturer's instructions for 30 minutes on ice. Cells were spun down and resuspended in neutral-buffered formalin for 10 minutes on ice for fixation. Cells were then resuspended in 100 μL PBS and analyzed on the Amnis CellStream flow cytometer (Luminex). A compensation matrix was generated using single-stained cells and an all dead sample generated from incubation in 70% ice-cold methanol in PBS for 10 minutes. Cells were gated on live and single cells. The compensation matrix and data analysis were performed using FlowJo software. Fluorescence intensity was plotted normalized to the mode for each sample.

Metabolic flux analysis. Mitochondrial oxidative phosphorylation was evaluated through the real-time measurement of the oxygen consumption rate (OCR) and glycolysis through the measurement of the extracellular acidification rate (ECAR) using the Seahorse XFe96 Extracellular Flux Analyzer (Agilent) at the Vanderbilt High Throughput Screening Core. For fibroblast experiments, NIH 3T3 cells irradiated to a dose of 10 Gy (1,500 cells/well) or unirradiated cells (2,200 cells/well) were seeded in an XFe96 culture microplate (Agilent 101085-004) and incubated overnight in normal growth media. Five hours prior to the experiment, cells were incubated with basal fibroblast media with either 100 μM CQ, equivalent volume of PBS, or 40 μM etomoxir for FAO inhibition. One-hour prior to calibration, following the manufacturer's instructions, the sensor cartridge from the Extracellular Flux Assay Kit (Agilent) was hydrated in sterilized DI water overnight at 37°C in a non-CO_2 incubator. One hour prior to the experiment, the cartridge was incubated with Seahorse XF Calibrant (Agilent 100840-000). Prior to loading cell plates, fibroblasts were washed in PBS and incubated for 1 hour in a non-CO_2 incubator in XF DMEM Medium, pH 7.4 (Agilent 103575-100) supplemented with 2.0 mM L-glutamine (Sigma G8540), 1.0 mM sodium pyruvate (Sigma S8636), and 10 mM D-(+)-glucose (Sigma G7528). For TNBC cell experiments, 4T1s were seeded at 5,000 cells/well directly in fibroblast CM 24 hours prior to the assay. The Seahorse XF Cell Mito Stress Test Kit (Agilent 103015-100) or the Seahorse XF Glycolysis Stress Test Kit (Agilent 103020-100) were then performed, and injection strategies were followed per the manufacturer's instructions with the exception of adding an initial PBS or media injection to establish baseline OCR and ECAR. The following final concentrations of injected drugs are as follows: 1.5 μM oligomycin to block ATP synthase for both 4T1s and 3T3s, 1.0 μM (3T3s) and 2.9 μM (4T1s) carbonyl cyanide-p-trifluoromethoxyphenylhydrazone FCCP to demonstrate maximal respiration, and a 0.5 μM mixture of rotenone and antimycin A for both cell types. Cells were counted following the experiment to normalize data per 1,000 cells. Data were analyzed using Seahorse Wave Desktop Software (Agilent), where a background well correction was applied. ATP-linked respiration was calculated as the difference between the baseline and post-oligomycin injected OCRs. OCR and ECAR time plots shown are representative biological replicates.

Intracellular pyruvate. 4T1 cells were analyzed for intracellular pyruvate pools. Cell lysates were collected after cells were plated in tissue-culture treated 6-well plates, washed with ice-cold PBS, and incubated with RIPA Buffer (Sigma R0278) containing 5 mM EDTA (Corning 46-034-CI), 1 EDTA-free mini cOmplete EASYpack tablet (Roche 04693159001), and 1 mini PhoSTOP EASYpack tablet (Roche 04906845001). Following cell lysis, supernatant was collected,

incubated on ice for 30 minutes, and spun down at 4°C (Fisher Scientific accuSpin Micro 17R). Supernatant was collected and stored at -80°C until use. Intracellular pyruvate concentrations were determined by using the pyruvate analysis component of the EnzyChrom Aspartate Assay Kit (Bioassay Systems EASP100) following the manufacturer's instructions. Concentrations were normalized to total protein determined from a Pierce BCA protein assay kit (Thermo Scientific 23227).

Lactate uptake inhibition. AZD3965 (MedChemExpress HY-12750) was used to inhibit lactate uptake in 4T1 cells. To determine the appropriate concentration, cells were incubated in RPMI 1640 containing no D-glucose or pyruvate (Gibco 11879-020) and 10 mM L-lactic acid sodium salt (Acros Organics 439220100) with increasing concentrations of AZD3965 (0.005 - 10 µM) or DMSO controls for 7 hours. Cell media was collected, and the remaining lactate concentration was determined using an EnzyFluo™ L-lactate assay kit (Bioassay Systems EFLLC-100) following the manufacturer's instructions. To evaluate the initial impact of AZD3965 on 4T1 cell proliferation, cells were incubated for 24 hours in basal 4T1 media with varying concentrations of AZD3965 in a 24-well tissue-culture treated plate, at which point bioluminescence imaging was performed. Total flux for each AZD3965 concentration was normalized to the total flux for cells incubated with a DMSO control.

Co-culture. To straddle the 7-day post-RT timepoint, we began a co-culture of $4T1^{luc}$ cells with irradiated or unirradiated fibroblasts at the 6-day post-RT timepoint. Co-culture was then performed for 48 hours in 6 well tissue culture treated plates. Seeding densities of fibroblasts were adjusted so that the same number of irradiated or unirradiated fibroblasts were present at the end of the 48-hour co-culture period. As a gauge for cell density, bioluminescence imaging was performed, and the total flux of the co-culture was normalized to total flux of $4T1^{luc}$ cells in basal fibroblast media.

Scratch wound assay. 4T1 cells were plated in 2-well culture inserts in µ-dishes (Ibidi 81176) at $3x10^5$ cells/mL in normal culture media for 24 hours, after which inserts were removed to create a cell-free gap representing the wound scratch. The µ-dishes were washed with PBS and incubated with either basal fibroblast media or 7-day post-RT 3T3 CM supplemented with 50 nM AZD3965, DMSO (control), or 5 mM L-lactate. Phase contrast images (16x) were taken every 3 hours until 15 hours total had elapsed. Scratch wound area was calculated in ImageJ as the cell-free space between the leading edge of the cells. Scratch wound closure percentage was

calculated by dividing scratch wound area by the area at the start of the assay.

Statistical analysis. Specific statistical tests for indicated datasets are indicated in figure captions. All analyses were performed using Minitab 18 or GraphPad Prism 8.

Disclosure of Potential Conflicts of Interest

No potential conflicts of interest were disclosed by the authors.

Author Contributions

Conception and design: KC Corn, M Rafat
Development of methodology: KC Corn, M Rafat
Acquisition of data: KC Corn, LS Britto, YK Mohamed, YI Ivanova
Analysis and interpretation of data: KC Corn, LS Britto, YK Mohamed, YI Ivanova, M Rafat
Writing, review, and/or revision of the manuscript: KC Corn, LS Britto, M Rafat
Study supervision: M Rafat

Acknowledgments

The authors thank Dr. Christopher Contag for generously providing luciferase-labeled 4T1s, Dr. Craig Duvall for the use of the IVIS, Dr. Michael Freeman for the use of the Cesium irradiator, and the Vanderbilt University High Throughput Screening core for use of the Seahorse XFe96 Metabolic Flux Analyzer. We would also like to thank Dr. Rachelle Johnson for her guidance in accessing and analyzing TCGA BRCA data. This research was financially supported by NIH grant #R00CA201304, the American Cancer Society Research Scholar Grant, the Ruth L. Kirschstein National Research Service Award grant #T32DK101003 (KCC), and the Maximizing Access to Research Careers Award grant #T34GM136451 (LSB). Visual schematics were prepared by the authors using BioRender.

References

1. Sung, H., Ferlay, J., Siegel, R. L., Laversanne, M., Soerjomataram, I., Jemal, A. & Bray, F. Global Cancer Statistics 2020: GLOBOCAN Estimates of Incidence and Mortality Worldwide for 36 Cancers in 185 Countries. *CA. Cancer J. Clin.* **71**, 209–249 (2021).
2. Sioshansi, S., Ehdaivand, S., Cramer, C., Lomme, M. M., Price, L. L. & Wazer, D. E. Triple negative breast cancer is associated with an increased risk of residual invasive carcinoma after lumpectomy. *Cancer* **118**, 3893–3898 (2012).
3. Siegel, R. L., Miller, K. D. & Jemal, A. Cancer statistics, 2019. *CA. Cancer J. Clin.* **69**, 7–34 (2019).
4. Wapnir, I. L. & Khan, A. Current Strategies for the Management of Locoregional Breast Cancer Recurrence. *Oncol. (willist. Park.* **33**, 19–25 (2019).
5. Smith, B. D., Bellon, J. R., Blitzblau, R., Freedman, G., Haffty, B., Hahn, C., Halberg, F., Hoffman, K., Horst, K., Moran, J., Patton, C., Perlmutter, J., Warren, L., Whelan, T., Wright, J. L. & Jagsi, R. Radiation therapy for the whole breast: Executive summary of an American Society for Radiation Oncology (ASTRO) evidence-based guideline. *Pract. Radiat. Oncol.* **8**, 145–152 (2018).
6. Darby, S., McGale, P., Correa, C., Taylor, C., Arriagada, R., Clarke, M., Cutter, D., Davies, C., Ewertz, M., Godwin, J., Gray, R., Pierce, L., Whelan, T., Wang, Y., Peto, R., Albain, K., Anderson, S., Arriagada, R., Barlow, W., *et al.* Effect of radiotherapy after breast-conserving surgery on 10-year recurrence and 15-year breast cancer death: Meta-analysis of individual patient data for 10 801 women in 17 randomised trials. *Lancet* **378**, 1707–1716 (2011).
7. David Voduc, K., Cheang, M. C. U., Tyldesley, S., Gelmon, K., Nielsen, T. O. & Kennecke, H. Breast Cancer Subtypes and the Risk of Local and Regional Relapse. *J. Clin. Oncol.* **28**, 1684–1691 (2010).
8. Adra, J., Lundstedt, D., Killander, F., Holmberg, E., Haghanegi, M., Kjellén, E., Karlsson, P. & Alkner, S. Distribution of Locoregional Breast Cancer Recurrence in Relation to Postoperative Radiation Fields and Biological Subtypes. *Int. J. Radiat. Oncol.* **105**, 285–295 (2019).
9. Lowery, A. J., Kell, M. R., Glynn, R. W., Kerin, M. J. & Sweeney, K. J. Locoregional recurrence after breast cancer surgery: a systematic review by receptor phenotype. *Breast Cancer Res. Treat.* **133**, 831–841 (2012).
10. Zhang, C., Wang, S., Israel, H. P., Yan, S. X., Horowitz, D. P., Crockford, S., Gidea-Addeo, D., Clifford Chao, K. S., Kalinsky, K. & Connolly, E. P. Higher locoregional recurrence rate

for triple-negative breast cancer following neoadjuvant chemotherapy, surgery and radiotherapy. *Springerplus* **4**, 1–9 (2015).

11. Havas, K. M., Milchevskaya, V., Radic, K., Alladin, A., Kafkia, E., Garcia, M., Stolte, J., Klaus, B., Rotmensz, N., Gibson, T. J., Burwinkel, B., Schneeweiss, A., Pruneri, G., Patil, K. R., Sotillo, R. & Jechlinger, M. Metabolic shifts in residual breast cancer drive tumor recurrence. *J. Clin. Invest.* **127**, 2091–2105 (2017).
12. Corn, K. C., Windham, M. A. & Rafat, M. Lipids in the tumor microenvironment: From cancer progression to treatment. *Prog. Lipid Res.* **80**, 101055 (2020).
13. Han, S., Wei, R., Zhang, X., Jiang, N., Fan, M., Huang, J. H., Xie, B., Zhang, L., Miao, W., Butler, A. C.-P., Coleman, M. A., Vaughan, A. T., Wang, Y., Chen, H.-W., Liu, J. & Li, J. J. CPT1A/2-Mediated FAO Enhancement—A Metabolic Target in Radioresistant Breast Cancer. *Front. Oncol.* **9**, (2019).
14. Du, Q., Tan, Z., Shi, F., Tang, M., Xie, L., Zhao, L., Li, Y., Hu, J., Zhou, M., Bode, A., Luo, | Xiangjian & Cao, Y. PGC1α/CEBPB/CPT1A axis promotes radiation resistance of nasopharyngeal carcinoma through activating fatty acid oxidation. *Cancer Sci.* **110**, 2050–2062 (2019).
15. Tan, Z., Xiao, L., Tang, M., Li, J., Li, L., Shi, F., Li, N., Li, Y., Du, Q., Lu, J., Weng, X., Yi, W., Zhang, H., Fan, J., Zhou, J., Gao, Q., Onuchic, J. N., Bode, A. M., Luo, X., *et al.* Targeting CPT1A-mediated fatty acid oxidation sensitizes nasopharyngeal carcinoma to radiation therapy. *Theranostics* **8**, 2329–2347 (2018).
16. Chuang, H.-Y., Lee, Y.-P., Lin, W.-C., Lin, Y.-H. & Hwang, J.-J. Fatty Acid Inhibition Sensitizes Androgen-Dependent and -Independent Prostate Cancer to Radiotherapy via FASN/NF-κB Pathway. *Sci. Rep.* **9**, (2019).
17. Göttgens, E.-L., van den Heuvel, C. N., de Jong, M. C., Kaanders, J. H., Leenders, W. P., Ansems, M., Bussink, J. & Span, P. N. ACLY (ATP Citrate Lyase) Mediates Radioresistance in Head and Neck Squamous Cell Carcinomas and is a Novel Predictive Radiotherapy Biomarker. *Cancers (Basel).* **11**, 1971 (2019).
18. Rafat, M., Aguilera, T. A., Vilalta, M., Bronsart, L. L., Soto, L. A., von Eyben, R., Golla, M. A., Ahrari, Y., Melemenidis, S., Afghahi, A., Jenkins, M. J., Kurian, A. W., Horst, K. C., Giaccia, A. J. & Graves, E. E. Macrophages Promote Circulating Tumor Cell–Mediated Local Recurrence following Radiotherapy in Immunosuppressed Patients. *Cancer Res.* **78**, 4241–4252 (2018).
19. Vilalta, M., Rafat, M., Giaccia, A. J. & Graves, E. E. Recruitment of Circulating Breast Cancer Cells Is Stimulated by Radiotherapy. *Cell Rep.* **8**, 402–409 (2014).

20. Dheeraj, A., Agarwal, C., Schlaepfer, I. R., Raben, D., Singh, R., Agarwal, R. & Deep, G. A novel approach to target hypoxic cancer cells via combining β-oxidation inhibitor etomoxir with radiation. *Hypoxia* **6**, 23–33 (2018).
21. Sawyer, B. T., Qamar, L., Yamamoto, T. M., McMellen, A., Watson, Z. L., Richer, J. K., Behbakht, K., Schlaepfer, I. R. & Bitler, B. G. Targeting Fatty Acid Oxidation to Promote Anoikis and Inhibit Ovarian Cancer Progression. *Mol. cancer Res.* **18**, 1088–1098 (2020).
22. Wang, Y. nan, Zeng, Z. lei, Lu, J., Wang, Y., Liu, Z. xian, He, M. ming, Zhao, Q., Wang, Z. xian, Li, T., Lu, Y. xin, Wu, Q. nian, Yu, K., Wang, F., Pu, H. Y., Li, B., Jia, W., Shi, M., Xie, D., Kang, T. bang, *et al.* CPT1A-mediated fatty acid oxidation promotes colorectal cancer cell metastasis by inhibiting anoikis. *Oncogene* **37**, 6025–6040 (2018).
23. Rodemann, H. P. & Bamberg, M. Cellular basis of radiation-induced fibrosis. *Radiother. Oncol.* **35**, 83–90 (1995).
24. Sumbal, J., Belisova, D. & Koledova, Z. Fibroblasts: The grey eminence of mammary gland development. *Semin. Cell Dev. Biol.* **114**, 134–142 (2021).
25. Parmar, H. & Cunha, G. R. Epithelial-stromal interactions in the mouse and human mammary gland in vivo. *Endocr. Relat. Cancer* **11**, 437–458 (2004).
26. Santi, A., Caselli, A., Ranaldi, F., Paoli, P., Mugnaioni, C., Michelucci, E. & Cirri, P. Cancer associated fibroblasts transfer lipids and proteins to cancer cells through cargo vesicles supporting tumor growth. *Biochim. Biophys. Acta - Mol. Cell Res.* **1853**, 3211–3223 (2015).
27. Auciello, F. R., Bulusu, V., Oon, C., Tait-Mulder, J., Berry, M., Bhattacharyya, S., Tumanov, S., Allen-Petersen, B. L., Link, J., Kendsersky, N. D., Vringer, E., Schug, M., Novo, D., Hwang, R. F., Evans, R. M., Nixon, C., Dorrell, C., Morton, J. P., Norman, J. C., *et al.* A Stromal Lysolipid–Autotaxin Signaling Axis Promotes Pancreatic Tumor Progression. *Cancer Discov.* **9**, 617–627 (2019).
28. Liu, G., Feng, S., Jia, L., Wang, C., Fu, Y. & Luo, Y. Lung fibroblasts promote metastatic colonization through upregulation of stearoyl-CoA desaturase 1 in tumor cells. *Oncogene* **37**, 1519–1533 (2018).
29. Neuwirt, H., Bouchal, J., Kharaishvili, G., Ploner, C., Jöhrer, K., Pitterl, F., Weber, A., Klocker, H. & Eder, I. E. Cancer-associated fibroblasts promote prostate tumor growth and progression through upregulation of cholesterol and steroid biosynthesis. *Cell Commun. Signal.* **18**, 11 (2020).
30. Martinez-Outschoorn, U. E., Lisanti, M. P. & Sotgia, F. Catabolic cancer-associated fibroblasts transfer energy and biomass to anabolic cancer cells, fueling tumor growth. *Semin. Cancer Biol.* **25**, 47–60 (2014).

31. Becker, L. M., O'Connell, J. T., Vo, A. P., Cain, M. P., Tampe, D., Bizarro, L., Sugimoto, H., McGow, A. K., Asara, J. M., Lovisa, S., McAndrews, K. M., Zielinski, R., Lorenzi, P. L., Zeisberg, M., Raza, S., LeBleu, V. S. & Kalluri, R. Epigenetic Reprogramming of Cancer-Associated Fibroblasts Deregulates Glucose Metabolism and Facilitates Progression of Breast Cancer. *Cell Rep.* **31**, 107701 (2020).
32. Zhao, X., Psarianos, P., Ghoraie, L. S., Yip, K., Goldstein, D., Gilbert, R., Witterick, I., Pang, H., Hussain, A., Lee, J. H., Williams, J., Bratman, S. V., Ailles, L., Haibe-Kains, B. & Liu, F.-F. Metabolic regulation of dermal fibroblasts contributes to skin extracellular matrix homeostasis and fibrosis. *Nat. Metab.* **1**, 147–157 (2019).
33. Sztalryd, C. & Brasaemle, D. L. The perilipin family of lipid droplet proteins: Gatekeepers of intracellular lipolysis. *Biochim. Biophys. Acta - Mol. Cell Biol. Lipids* **1862**, 1221–1232 (2017).
34. Goldman, M. J., Craft, B., Hastie, M., Repečka, K., McDade, F., Kamath, A., Banerjee, A., Luo, Y., Rogers, D., Brooks, A. N., Zhu, J. & Haussler, D. Visualizing and interpreting cancer genomics data via the Xena platform. *Nat. Biotechnol. 2020 386* **38**, 675–678 (2020).
35. Wilfling, F., Haas, J. T., Walther, T. C. & Jr, R. V. F. Lipid droplet biogenesis. *Curr. Opin. Cell Biol.* **29**, 39–45 (2014).
36. Katayama, I., Hotokezaka, Y., Matsuyama, T., Sumi, T. & Nakamura, T. Ionizing Radiation Induces Macrophage Foam Cell Formation and Aggregation Through JNK-Dependent Activation of CD36 Scavenger Receptors. *Int. J. Radiat. Oncol. Biol. Phys.* **70**, 835–846 (2008).
37. Gao, F., Liu, C., Guo, J., Sun, W., Xian, L., Bai, D., Liu, H., Cheng, Y., Li, B., Cui, J., Zhang, C. & Cai, J. Radiation-driven lipid accumulation and dendritic cell dysfunction in cancer. *Sci. Rep.* **5**, (2015).
38. Huang, Y. H., Yang, P. M., Chuah, Q. Y., Lee, Y. J., Hsieh, Y. F., Peng, C. W. & Chiu, S. J. Autophagy promotes radiation-induced senescence but inhibits bystander effects in human breast cancer cells. *Autophagy* **10**, 1212–1228 (2014).
39. Wang, X., Zhang, J., Fu, J., Wang, J., Ye, S., Liu, W. & Shao, C. Role of ROS-mediated autophagy in radiation-induced bystander effect of hepatoma cells. *Int. J. Radiat. Biol.* **91**, 452–458 (2015).
40. Nguyen, T. B., Louie, S. M., Daniele, J. R., Tran, Q., Dillin, A., Zoncu, R., Nomura, D. K. & Olzmann, J. A. DGAT1-Dependent Lipid Droplet Biogenesis Protects Mitochondrial Function during Starvation-Induced Autophagy. *Dev. Cell* **42**, 9-21.e5 (2017).

41. Mizushima, N., Yoshimori, T. & Levine, B. Methods in Mammalian Autophagy Research. *Cell* **140**, 313–326 (2010).
42. Runwal, G., Stamatakou, E., Siddiqi, F. H., Puri, C., Zhu, Y. & Rubinsztein, D. C. LC3-positive structures are prominent in autophagy-deficient cells. *Sci. Rep.* **9**, 1–14 (2019).
43. Endo, K., Katsuyama, Y., Taira, N., Yoshioka, M., Okano, Y. & Masaki, H. Impairment of the autophagy system in repetitively UVA-irradiated fibroblasts. *Photodermatol. Photoimmunol. Photomed.* **36**, 111–117 (2020).
44. Mauro-Lizcano, M., Esteban-Martínez, L., Seco, E., Serrano-Puebla, A., Garcia-Ledo, L., Figueiredo-Pereira, C., Vieira, H. L. A. & Boya, P. New method to assess mitophagy flux by flow cytometry. *Autophagy* **11**, 833–843 (2015).
45. Xiao, B., Deng, X., Zhou, W. & Tan, E. K. Flow cytometry-based assessment of mitophagy using mitotracker. *Front. Cell. Neurosci.* **10**, 1–4 (2016).
46. Draoui, N. & Feron, O. Lactate shuttles at a glance: from physiological paradigms to anti-cancer treatments. *Dis. Model. Mech.* **4**, 727–732 (2011).
47. Benyahia, Z., Blackman, M. C. N. M., Hamelin, L., Zampieri, L. X., Capeloa, T., Bedin, M. L., Vazeille, T., Schakman, O. & Sonveaux, P. In Vitro and In Vivo Characterization of MCT1 Inhibitor AZD3965 Confirms Preclinical Safety Compatible with Breast Cancer Treatment. *Cancers 2021, Vol. 13, Page 569* **13**, 569 (2021).
48. Kuo, L. J. & Yang, L.-X. Gamma-H2AX - a novel biomarker for DNA double-strand breaks. *In Vivo (Brooklyn).* **22**, 305–9 (2008).
49. Kinner, A., Wu, W., Staudt, C. & Iliakis, G. Gamma-H2AX in recognition and signaling of DNA double-strand breaks in the context of chromatin. *Nucleic acids research* vol. 36 5678–5694 (2008).
50. Qiu, B. & Simon, M. C. BODIPY 493/503 Staining of Neutral Lipid Droplets for Microscopy and Quantification by Flow Cytometry. *Bio-protocol* **6**, (2016).
51. Somwar, R., Roberts, C. T. & Varlamov, O. Live-cell imaging demonstrates rapid cargo exchange between lipid droplets in adipocytes. *FEBS Lett.* **585**, 1946–1950 (2011).
52. Klionsky, D. J., Abdelmohsen, K., Abe, A., Joynal Abedin, M., Abeliovich, H., Acevedo Arozena, A., Adachi, H., Adams, C. M., Adams, P. D., Adeli, K., Adhihetty, P. J., Adler, S. G., Agam, G., Agarwal, R., Aghi, M. K., Agnello, M., Agostinis, P., Aguilar, P. V, Aguirre-Ghiso, J., *et al.* Guidelines for the use and interpretation of assays for monitoring autophagy (3rd edition). *Autophagy* **12**, 1–222 (2016).

Figures

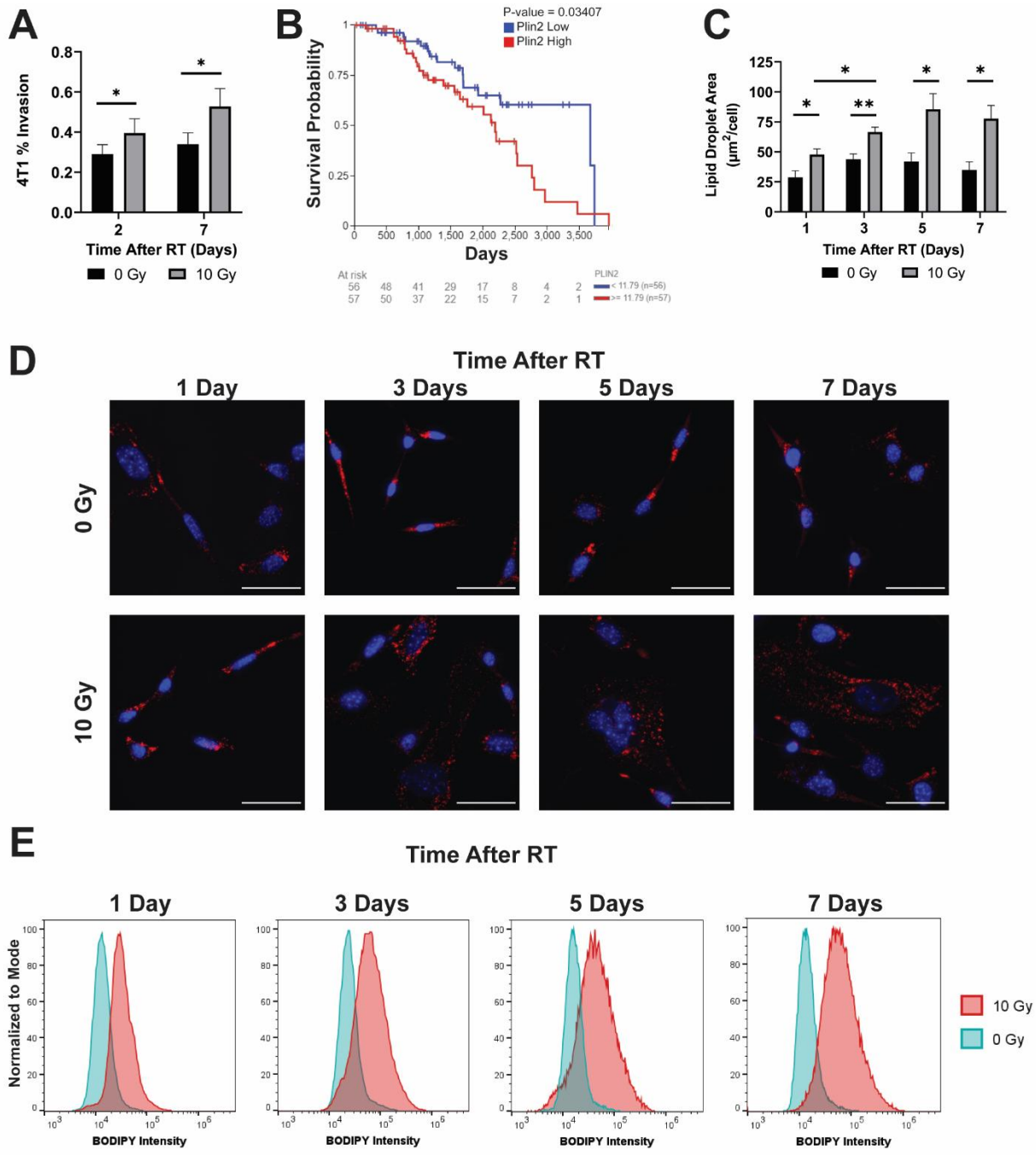

Figure 1. Radiation increases lipid droplets in 3T3 fibroblasts. **(A)** Conditioned media (CM) collected from irradiated fibroblasts at 2- and 7-days post-RT increased the invasiveness of 4T1 TNBC cells in a transwell assay (n = 5). Statistical significance was determined by a paired t-test

with *p<0.05. **(B)** Kaplan-Meier analysis of overall survival utilizing NAT data from the TCGA BRCA dataset accessed through UCSC's Xena platform[34] and grouping patients based on high or low *Plin2* gene expression. Statistical analysis performed using the log-rank test. **(C)** Quantification of the cross-sectional area of lipid droplets from perilipin-2 immunofluorescence staining (n = 5). Statistical significance was determined by an unpaired t-test with *p<0.05 and **p<0.01. **(D)** Representative images of fibroblasts stained with perilipin-2 (red) and counterstained with NucBlue up to 7-days post-RT. Scale bar is 40 μm. **(E)** Representative flow cytometry analysis of BODIPY-stained fibroblasts in control (blue) and irradiated (red) cells up to 7 days post-RT (n = 3). Error bars show SEM.

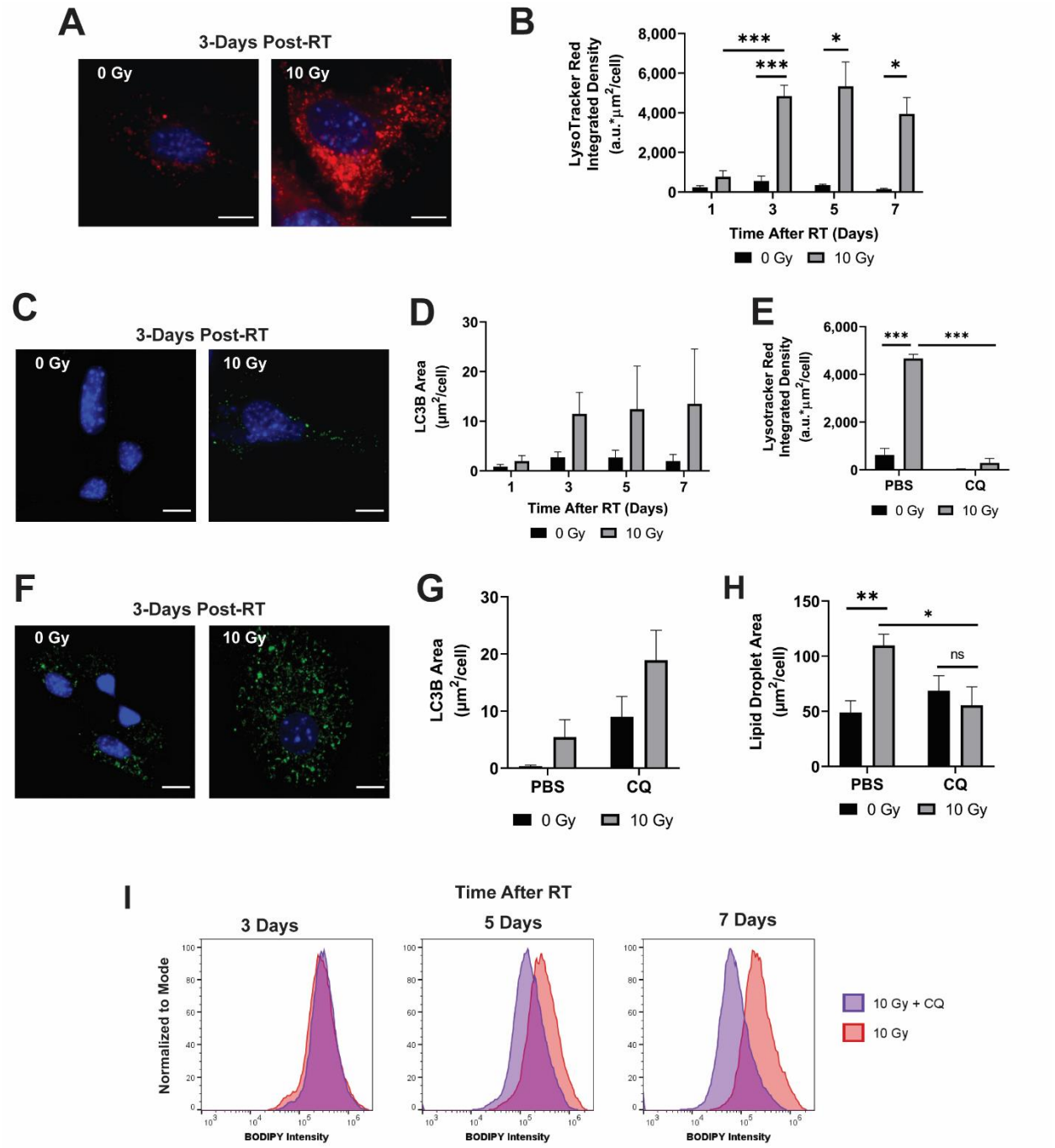

Figure 2. Radiation induces prolonged autophagy upregulation in fibroblasts and promotes lipid droplet formation. **(A)** Representative images of LysoTracker Red DND-99 staining with NucBlue counterstaining in irradiated and control fibroblasts 3-days post-RT. Scale bar is 10 µm. **(B)** Quantification of live-cell lysosomal staining in irradiated and control fibroblasts (n = 4). **(C)** Representative images of LC3B staining (green) with NucBlue counterstaining (blue) 3-days post-RT. Autophagosomes are identified by the formation of bright LC3B puncta. Scale bar is 30 µm. **(D)** Quantification of autophagosome cross-sectional area per cell in irradiated and

control fibroblasts (n = 5). **(E)** Quantification of live cell lysosomal staining in irradiated and control fibroblasts following CQ incubation or PBS control 3-days post-RT (n = 3). **(F)** Representative images of LC3B staining (green) with NucBlue counterstaining (blue) in irradiated and unirradiated fibroblasts 3-days post-RT following autophagy inhibition with CQ (n = 3). Scale bar is 30 μm. Corresponding quantification of autophagosomal cross-sectional area per cell in irradiated and control fibroblasts **(G)** and the cross-sectional area of lipid droplets from perilipin-2 staining with either CQ or PBS incubation **(H)**. **(I)** Representative flow cytometry analysis of BODIPY-stained irradiated fibroblasts with 100 μM CQ inhibition (purple) or uninhibited (red) up to 7 days post-RT. Error bars show SEM. Statistical analysis was determined by an unpaired two-tailed t-test with *$p<0.05$ and ***$p<0.001$.

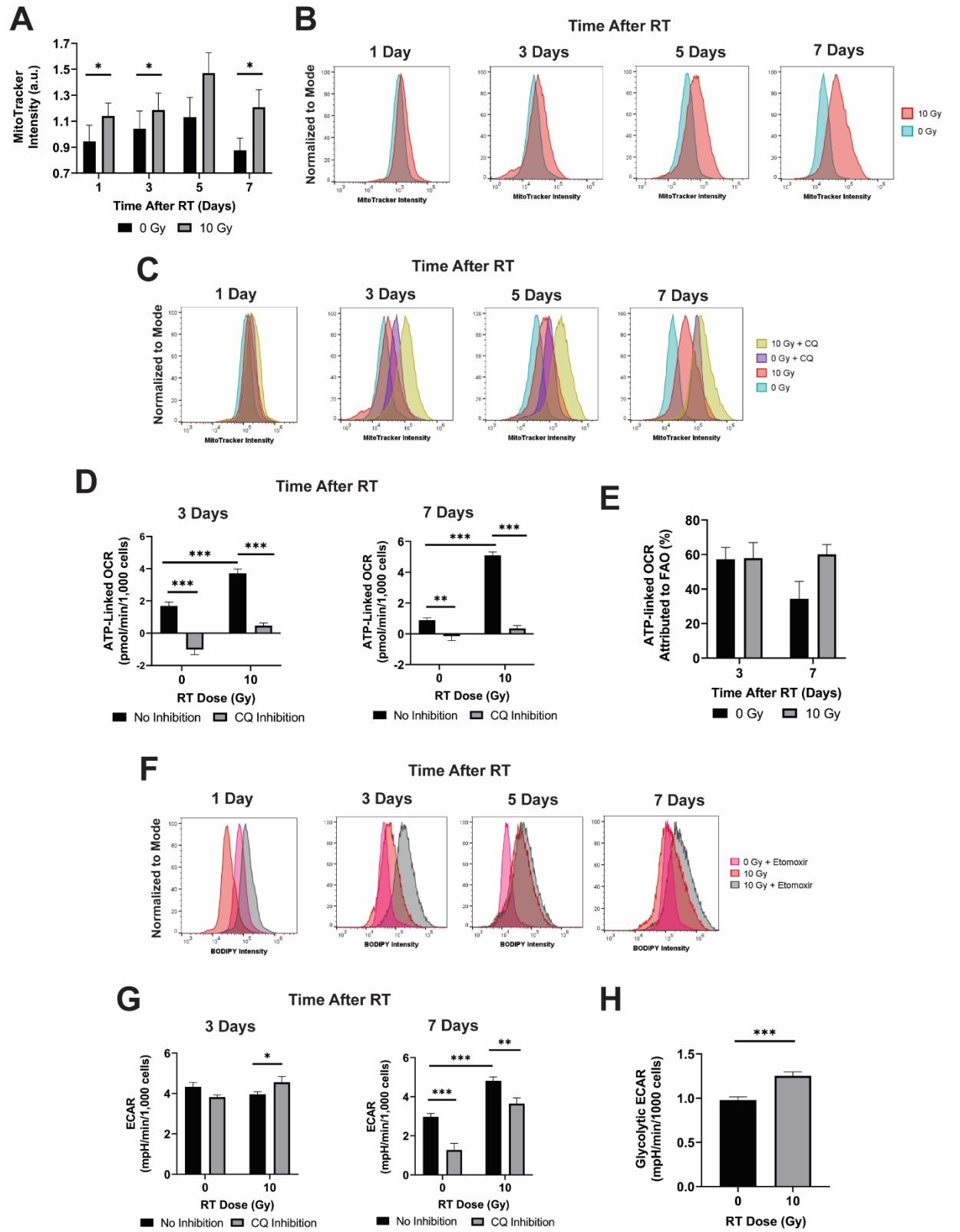

Figure 3. Radiation-induced autophagy impacts mitochondrial energetics and aerobic glycolysis. (A) Normalized MitoTracker Deep Red live-cell fluorescence intensity in irradiated

and unirradiated fibroblasts up to 7-days post-RT (n = 4). **(B)** Representative flow cytometry analysis of MitoTracker Deep Red-stained irradiated and unirradiated fibroblasts up to 7-days post-RT. **(C)** Representative flow cytometry analysis of MitoTracker Deep Red-stained irradiated and unirradiated fibroblasts with and without CQ inhibition up to 7-days post-RT. **(D)** ATP-linked OCR in irradiated and unirradiated fibroblasts at 3-days and 7-days post-RT with and without CQ inhibition. **(E)** Percent of ATP-linked OCR attributed to FAO in irradiated and unirradiated fibroblasts and 3-days and 7-days post-RT. **(F)** Representative flow cytometry analysis of BODIPY-stained fibroblasts with and without etomoxir incubation up to 7-days post-RT. **(G)** Baseline ECAR in irradiated and unirradiated fibroblasts at 3-days and 7-days post-RT with and without CQ inhibition. **(H)** Glycolytic-linked ECAR in 7-day post-RT irradiated and unirradiated fibroblasts. Error bars show SEM. Statistical analysis was determined by an unpaired two-tailed t-test with *$p<0.05$, **$p<0.01$, and ***$p<0.001$.

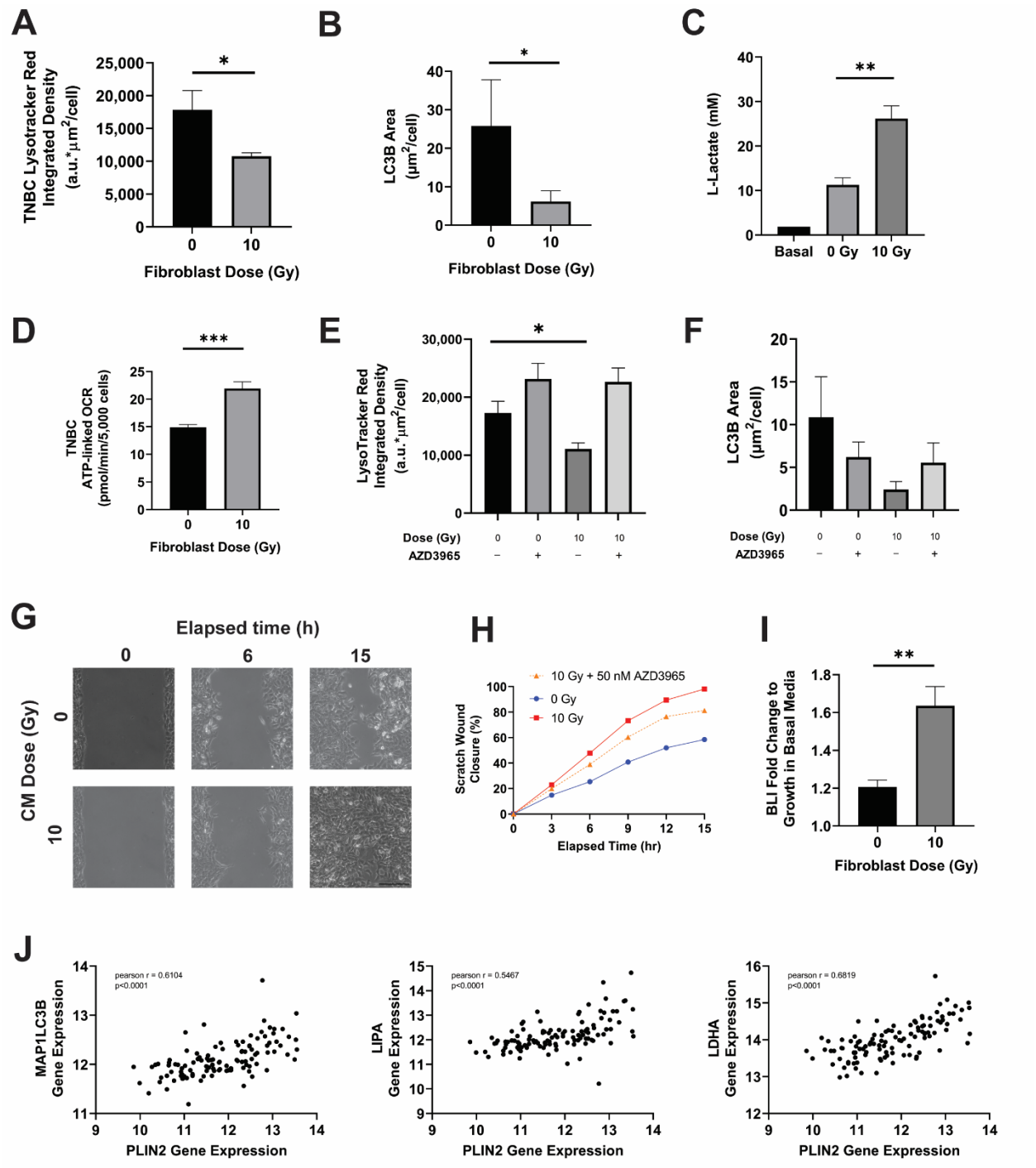

Figure 4. **Radiation-induced aerobic glycolysis of fibroblasts results in lactate metabolic crosstalk with breast cancer cells. (A)** Quantification of live-cell lysosomal staining in TNBC cells incubated with irradiated or unirradiated 7-day post-RT fibroblast CM (n = 3). **(B)** Quantification of autophagosomal cross-sectional area per cell in TNBC cells incubated with irradiated or unirradiated 7-day post-RT fibroblast CM (n = 5). **(C)** Quantification of L-lactate

concentration in basal fibroblasts media and CM collected 7-days post-RT from irradiated and unirradiated fibroblasts (n = 4). **(D)** ATP-linked OCR in TNBC cells incubated for 24 hours in irradiated and unirradiated 7-day post-RT fibroblast CM. **(E)** Quantification of live-cell lysosomal staining in TNBC cells incubated with irradiated or unirradiated 7-day post-RT fibroblast CM and with either AZD3965 or DMSO control (n = 2 – 5). **(F)** Quantification of autophagosomal cross-sectional area per cell in TNBC cells incubated with irradiated or unirradiated 7-day post-RT fibroblast CM and with either AZD3965 or DMSO control (n = 3). **(G)** Representative images of 4T1 TNBC cells in scratch wound assays at 0-, 6-, and 15-hour timepoints following incubation in either irradiated or unirradiated 7-day post-RT fibroblast CM. Scale bar is 200 μm. **(H)** Quantification of the percent closure of the scratch wound gap for TNBC cells incubated in fibroblast CM (n = 1). **(I)** Normalized bioluminescent total flux of $4T1^{luc}$ cells co-cultured with either unirradiated or 6-day post-RT irradiated fibroblasts for 48 hours (n = 5). **(J)** *Plin2* expression in NAT gathered from the TCGA BRCA dataset[34] plotted against *Map1lc3b*, *Lipa*, and *Ldha* gene expression data with Pearson correlation coefficients (n = 113 patient samples). Error bars show SEM. Statistical analysis was determined by an unpaired two-tailed t-test with *p<0.05, **p<0.01, and ***p<0.001.